Cation-site intrinsic defects in Zn-doped CdTe

A. Carvalho,[1,2] A. K. Tagantsev,[2] S. Öberg,[3] P. R. Briddon,[4] and N. Setter[2]
[1]*School of Physics, University of Exeter, Exeter EX4 4QL, United Kingdom*
[2]*Ceramics Laboratory, Swiss Federal Institute of Technology (EPFL), CH-1015 Lausanne, Switzerland*
[3]*Department of Mathematics, Luleå University of Technology, Luleå S-97187, Sweden*
[4]*School of Electrical, Electronic and Computer Engineering, University of Newcastle upon Tyne, Newcastle upon Tyne, NE1 7RU England, United Kingdom*
(Received 15 October 2009; revised manuscript received 29 January 2010; published 26 February 2010)

The properties of the cation vacancy and the Te antisite, two dominant defects in CdTe and $Cd_{1-x}Zn_xTe$ alloys grown in Te-rich conditions, are examined using first-principles calculations. First, the structure, electronic levels, and migration paths of V_{Cd} and Te_{Cd} in CdTe are studied in detail. Additionally, we analyze the evolution of the stability and electronic properties in $Cd_{1-x}Zn_xTe$ alloys, taking into account both the role of alloying in the position of the ionization levels and its effects on the equilibrium concentration of those two defects. It is shown that the formation of cation vacancies becomes progressively more favorable as x increases, whereas Te antisites become less stable, backing the trend towards p-type conductivity in dilute $Cd_{1-x}Zn_xTe$.

DOI: 10.1103/PhysRevB.81.075215 PACS number(s): 71.55.Gs, 72.80.Ey

I. INTRODUCTION

Its large band gap, high absorption coefficient and high intrinsic resistivity place CdTe and its alloys amongst the most promising materials for optoelectronic applications. These include x- and gamma-ray detectors, nonlinear optical devices, and high efficiency solar cells.[1–3] $Cd_{1-x}Zn_xTe$ alloys offer the possibility of engineering the optical properties of the material, in particular, tailoring the band-gap energy to the requirements of each specific application. The 1.5 eV band gap of CdTe is an ideal match to the solar spectrum, making it an extraordinary photovoltaic absorber.[4] In contrast, for detector applications, a larger band gap, obtained for a small fraction of Zn, allows a better performance at room temperature.[5] Doping with Zn opens yet another field of novel applications taking advantage of the unusual ferroelectriclike properties of the $Cd_{1-x}Zn_xTe$ system. Reported both in bulk samples[6–8] and in thin films[9] with up to 4% of Zn, ferroelectric characteristics include the temperature dependence of the dielectric constant and the observation of the hysteretic behavior of polarization and of the piezoelectric coefficient d_{33}. There is no parallel for this behavior in other zinc-blende semiconductors and it is still not clear whether this phenomena is a bulk property or it originates from defects incorporated in the material.

In fact, despite recent advances,[10] the growth of high-quality stoichiometric $Cd_{1-x}Zn_xTe$ alloys, with high resistivity and low defect density, is more difficult to achieve than for the end binary compounds.[11] Intrinsic defects and residual impurities invariably present in high-purity undoped CdTe and $Cd_{1-x}Zn_xTe$ materials typically are electrically active and the high resistivity required for detector applications is usually achieved by counter doping with group-VII elements or other donors.[12,13] Nevertheless, the performance of x- and gamma-ray detectors is compromised by the trapping of charge carriers at defects, resulting in incomplete charge collection.[14] Compensation by intrinsic defects also limits both the n- and p-type dopability, causing problems in making low-resistance ohmic contacts to the substrate in CdTe-based solar cells.[4] It order to control the defect density and charge-transport properties, it is desirable to obtain reliable information about the stability and ionization levels of point defects in CdTe and $Cd_{1-x}Zn_xTe$ alloys.

Unfortunately, although intrinsic point defects in CdTe have been object of extensive research in the last decades, their identification still remains controversial. Typically material grown by the Bridgeman technique is Te rich, with a high content of defects in the cation lattice.[15] From these, the most important are the cadmium vacancy (V_{Cd}) and the tellurium antisite (Te_{Cd}).[16] It is generally believed that V_{Cd} is an acceptor, the main responsible for the p-type conductivity of the as-grown material, whereas Te_{Cd} is a donor; however, there has been much discussion about their geometry and the position of the respective defect levels. Back to the 1990s, electron paramagnetic resonance (EPR) spectroscopy and electron-nuclear double resonance have found two centers which have originally been related to the Te vacancy (F center)[17–19] and the Cd vacancy.[18,20] The former, an isotropic center with an ionization energy of 0.2 eV, has subsequently been assigned to Te_{Cd}^{+} (Ref. 21) or even related to a similar oxygen-related defect.[22,23]

The EPR center initially attributed to V_{Cd}^{-},[17,20] a trigonal center with an unpaired electron localized on one Te atom, can be excited with light of photon energy equal or larger than 0.47 eV. Curiously, first-principles calculations of the hyperfine interactions of V_{Te} and V_{Cd} give no support to these two assignments.[24] Further, electronic-structure calculations give no indication of Jahn-Teller distortion which has been postulated for V_{Cd}^{-}.[20,25] Vacancy centers observed by perturbed angular γ-γ correlation (PAC) spectroscopy in Te-rich In-doped crystals suggest that V_{Cd}, as theory predicts, is present in three charge states, but no doubling of the signals is observed as would be expected for a anisotropic trigonal center.

Ionization levels possibly related to these two centers have been measured by other techniques, including Hall-effect measurements[26] thermoelectric effect spectroscopy (TEES),[14,27] modulated photocurrent,[21] admittance spectroscopy,[28] deep level transient spectroscopy (DLTS),[29] and photoinduced current transient spectroscopy (PICTS).[29]

TABLE I. Intrinsic defect levels in CdTe. Top: levels previously assigned to V_{Cd} and respective theoretical predictions; Bottom: levels previously assigned to Te_{Cd} and respective theoretical predictions. Defect levels in dilute $Cd_{1-x}Zn_xTe$ are marked with a note.

Method	Levels (eV)	References
Hall effect	E_v+0.05, E_c−(0.6–0.7)	26
EPR	E_v+0.47	18 and 20
TEES[a]	E_v+0.43	14
PAC, admittance	E_v+0.23	28
TEES	E_v+0.735	27
DLTS, PICTS	E_v+0.14, E_v+0.40, E_v+0.76	29
TEES	E_v+0.1, E_v+0.23	30
Theory	E_v+0.2, E_v+0.8	16
Theory	E_v+0.13, E_v+0.21	31
Theory	E_v+0.12, E_v+0.27	32
Theory	E_v+0.1, E_v+0.1–0.2	33
Theory	E_v+0.1, E_v+0.2	34

Method	Levels (eV)	References
EPR, MP	E_c−0.2	21
TEES	E_v+0.743	27
Deep level spectroscopy	E_c−0.75	35
Hall effect[b]	E_c−0.01, E_c−0.75	13
DLTS, PICTS	E_v+0.32	29
TEES	E_c−0.4	30
Theory	E_c−0.59, E_c−0.34	31

[a]Measured in $Cd_{0.88}Zn_{0.12}Te$.
[b]Measured in $Cd_{0.9}Zn_{0.1}Te$.

Some of these are summarized in Table I. The identity of these centers, usually suggested by an analysis of the conditions of formation, equilibrium charge state, and annealing behavior, is difficult to establish and the situation becomes even more complex in CdZnTe.

Previous theoretical calculations have placed the acceptor levels of V_{Cd} and Te_{Cd}, respectively, in the lower and upper halves of the band gap.[16,32,34] However, it has been difficult to establish a relation to the levels measured experimentally. Furthermore, little information has been provided on the evolution of the defect properties in CdZnTe alloys.

The present work aims to contribute to the identification and control of V_{Cd} and Te_{Cd} by presenting a comprehensive first-principles study of their properties in CdZnTe alloys with low Zn content. We first analyze in detail the geometry, stability, and electronic structure of these two defects in CdTe (Sec. III). Then we discuss how the addition of Zn changes these properties. Section IV focuses on the interaction between the defects and Zn atoms in the $x \to 0$ limit. Subsequently Sec. V will show, based both on local strain effect considerations and on a pseudorandom-alloy model, that the formation energy of the Cd vacancy decreases with increasing Zn content, whereas the formation energy of the Te antisite shows the opposite behavior. Section VI discusses the assignment of some of the defect centers reported by experimental studies to V_{Cd} and Te_{Cd}, and explains how the evolution of the conductivity type in $Cd_{1-x}Zn_xTe$ can be related to the density of intrinsic defects.

TABLE II. Basic properties of CdTe, ZnTe, and CdZnTe alloys: lattice parameters (a_0), relaxation parameters (ϵ), deviation from Vegard's law (γ), bulk modulus (B), band gap at $\Gamma(E_g)$, and valence-band shift (ΔE_v). For definitions of ϵ and γ, the reader is referred to Sec. V A. Representative values from other calculations and from experiment are given for comparison. Star (*) and double star (**) indicate, respectively, values obtained within discrete Fourier transformed using a gradient approximation (Ref. 41) or from GW calculations.

Property	This work	Previous work	Expt.
a_0^{CdTe}(Å)	6.447	6.470[e], 6.422[f], 6.626[f],*	6.43[d], 6.46–6.48[b],*
a_0^{ZnTe}(Å)	6.025	6.052[e], 6.017[e], 6.195[f],*	6.08[d],6.10[b]
$\epsilon_{Cd\text{-}Te}$	0.81		0.78[a]
$\epsilon_{Zn\text{-}Te}$	0.80		0.78[a]
$\gamma_{x=0.5}$	∼−0.007		
B^{CdTe} (GPa)	44	44.00[e]	42–45[c]
B^{ZnTe} (GPa)	53	52.10[e]	52.8
E_g^{CdTe} (eV)	0.60	0.61[f], 0.62[f],*, 1.2[g],**	1.44[d]
E_g^{ZnTe} (eV)	1.30	1.28[f], 1.14[f],*, 2.23[g],**	2.26[d]
ΔE_v (eV)	0.10	0.09[h]	

[a]X ray, Ref. 42.
[b]Augmented plane-wave (APW) calculation, Ref. 43.
[c]At 25 °C, from Ref. 44.
[d]Reference 45.
[e]APW calculation, from Ref. 46.
[f]All-electron calculation with Gaussian basis sets from Ref. 38.
[g]GW calculations, from Refs. 47 and 48.
[h]Reference 49.

II. METHODOLOGY

We performed spin-polarized pseudopotential calculations, carried out using the AIMPRO code.[36,37] For the exchange and correlation energy (E_{xc}), a local spin density approximation (LSDA) approximation was adopted. This functional yields accurately the structural properties of CdTe.[38] The core electrons were treated using the dual space separable pseudopotentials of Hartwigsen *et al.*[39] Spin-orbit coupling will be ignored in the present consideration. The Kohn-Sham functions were expanded in a basis of Cartesian Gaussian basis functions as described in Refs. 36 and 40. The charge density was expanded in a plane-wave basis set with 112 Ha of cutoff energy. Using this method, we obtain a good description of the basic properties of bulk CdTe and ZnTe, in agreement with previous calculations and with experiment (Table II).

The solid is described by imposing periodic boundary conditions. We employ cubic supercells containing a total of 64 up to 512 atoms, corresponding to a repetition of the conventional zinc-blende unit cell along the three lattice vectors (Cd_mTe_m). Supercells containing the defects will be

noted $Cd_mTe_m:D$, where D is the defect replacing one or more lattice atoms. We performed convergence studies with respect to the basis sets, supercell size, and number of points used for Brillouin zone (BZ) sampling to make sure that the conclusions were not affected by the methodology used. Convergence issues are presented in the Appendix.

Computation of formation energies

The formation of intrinsic defects is thermally activated and its concentration in equilibrium conditions $[D]$ can be related to the defect formation energy ΔG_D by

$$[D] = gN_D \exp\left(-\frac{\Delta G_D}{kT}\right), \quad (1)$$

where N_D is the number of sites available to the defect.

According to the thermodynamical definition, the formation energy of the defect depends on the chemical potential of its constituents,

$$\Delta G_D = G_D - \sum_i n_i\mu_i + q\mu_e, \quad (2)$$

where G_D is the free energy of the system containing the defect, n_i is the number of atoms of species i that it contains, and μ_i is the respective chemical potential. Additionally, the formation energy of a charged system, in charge state q, depends on the chemical potential of the electrons (μ_e).

The chemical potentials are defined by the experimental growth conditions, which can range from Cd rich to Te rich. They should therefore figure explicitly as variables in our formalism. However, it is useful to consider extreme conditions, which establish bounds for the chemical potentials of the elements and are useful to the interpretation of the results. For CdTe, the Cd-rich limit is defined by imposing an equilibrium between the system and a reservoir of Cd in the metallic form, whereas in Te-rich conditions μ_{Te} is fixed to its value in metallic tellurium. For $Cd_xZn_{1-x}Te$ alloys, we impose the condition that the system is homogeneous, i.e., there is no phase separation between CdTe and ZnTe. In this case, we evaluate formation energies only in the Te-rich limit.

The formation energy of the defect is obtained using a supercell model. As a working approximation, it is common to neglect vibrational entropy terms and calculate the formation energies at $T=0(E_f[D])$,

$$E_f[D^q] = E[Cd_mTe_m:D^q] - \sum_i n_i\mu_i + q(E_F + E_v), \quad (3)$$

where $E[Cd_mTe_m:D^q]$ is the energy of the $Cd_mTe_m:D^q$ supercell, and E_F is the Fermi level, defined relative to the valence-band top E_v. The value of E_v is obtained from the bulk supercell calculation, subsequently corrected for the different energy scales in the bulk and defective supercells. This correction is performed by aligning the average electrostatic potentials at the defective supercell at a (001) plane far from the defect and at an equivalent plane in the undefective neutral supercell.[50,51] Additionally, the energies of charged supercells were corrected for spurious electrostatic effects as discussed in the Appendix.

The thermodynamic transition level $E_D(q/q+1)$ can be defined as the value of the Fermi level for which charge states q and $q+1$ of the defect D have the same formation energy. We obtain $E_D(q/q+1)$ using the formation energy method. From Eq. (3),

$$E_D(q/q+1) = E[Cd_mTe_m:X^q] - E[Cd_mTe_m:X^{q+1}] - E_v. \quad (4)$$

III. CATION-SITE DEFECTS IN CdTe

We will analyze the geometry and electronic structure of the V_{Cd} and Te_{Cd} defects, their formation energies and preferred paths for migration.

A. Cadmium vacancy

Removing a Cd atom leaves four dangling bonds. The respective defect states can be regarded as sp^3 orbitals transforming as $t_2 \otimes a_1$ representations of the T_d point symmetry group. In addition to the two electrons of the Cd atom which has been removed, they were originally occupied by six electrons provided by the neighboring Te atoms. Upon the removal of one Cd, leaving a neutral vacancy, the valence shell of the next-neighbor Te atoms has a deficiency of two electrons, which is compensated by capturing two free electrons. Thus, the Cd vacancy is a double acceptor.

Now, the filling of the a_1 and t_2 states depends on their position with respect to the valence-band states where they originate from. The a_1 state is filled and sinks deep into the valence band. In the neutral charge state, the t_2 levels lie just above E_v, hybridizing with host states. The neutral defect has, in the tetrahedrally coordinated structure, a partially unoccupied level, which in principle could be sensitive to Jahn-Teller instability.

The deviation from tetrahedral symmetry can be quantified by minimizing the potential energy of the defect system along different directions of distortion. In order to find the ground-state electronic configurations of V_{Cd}^{0} and V_{Cd}^{-}, allowing the system to adopt a configuration of lower symmetry, we optimized the atomic coordinates using as starting point distorted structures with D_{2d}, C_{3v}, and C_1 symmetries, and different spin states.

The nonmagnetic and magnetic states of the neutral vacancy were found to be practically equivalent in energy. The D_{2d} and C_{3v} structures were only 0.01 eV lower in energy than the high-symmetry structure (in the 216 atom supercell), and the differences between the lengths of inequivalent bonds were less then 0.02 Å and close to the accuracy limit of our calculations. This result was independent of the supercell size and number of **k** points used for BZ sampling. In the negative charge state, the distortion energy was also immeasurable. In $V_{Cd}^{=}$, there is no electronic degeneracy associated with the t_2 level, for the number of electrons trapped at the defect equals the number of electrons donated by the original Cd atom.

The absence of strong distortion is a consequence of the position of the defect-related levels with respect with the bands of the host crystal. The Kohn-Sham band structure shows that the neutral defect introduces an unoccupied level

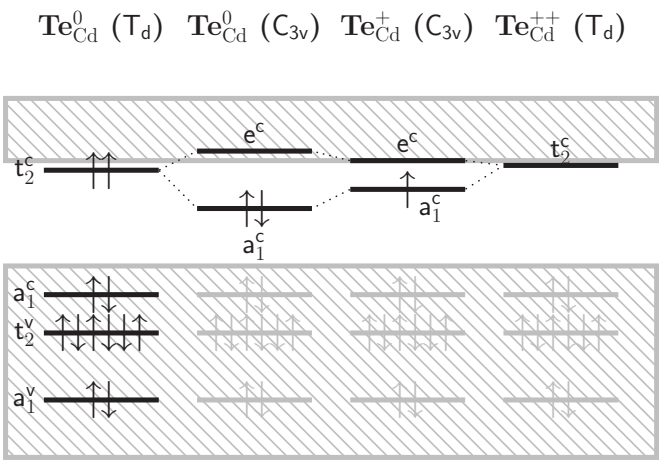

FIG. 1. LCAO model for the splitting of the Te_{Cd}-related levels (not to scale).

close to the valence-band top. This is a perturbed host state,[52] formed by a merging of the t_2 state from the Te dangling bonds into the valence-band states and its dispersion resembles that of the original valence-band top. As the electronic degeneracy is associated with delocalized states, with little influence in the binding of the vacancy nearest neighbors, the associated instability is very small. This result is in agreement with the conclusions of previous studies.[25,53,54]

B. Tellurium antisite

The scenario is different for the Te antisite. First, the four sp^3 bonds give rise to two $t_2 \otimes a_1$ sets of states. As the Te atom has an excess of four electrons with respect to the Cd it replaces for, the lower ${t_2}^v$ and ${a_1}^v$ are filled and remain in the valence band; however, depending on their occupation numbers, the ${t_2}^c$ and ${a_1}^c$ states, originating from the conduction-band states, may descend into the band gap and play an important role in the structure and electrical properties of the defect.

The ${t_2}^c$ level, lying in the band gap for the neutral T_d defect, is partially occupied (Fig. 1). The repulsion between its valence electrons and those of its neighbors drives an off-center displacement of the Te atom along the $\langle 111 \rangle$, lifting the electronic degeneracy and leaving a filled ${a_1}^c$ and an empty e^c state. Total-energy calculations show that for the neutral charge state, the C_{3v} configuration with occupations $({a_1}^c)^2(e^c)^0$ is 1.01 eV lower in energy than the undistorted paramagnetic $({t_2}^c)^2$ state (superscripts indicate the occupation of the single-electron states). An alternative $S=0$ cubic configuration with two electrons in the conduction band is about 1.14 eV higher in energy than the $({a_1}^c)^2(e^c)^0$ ground state. These stabilization energies are considerably higher than the 0.46 eV found by a previous study.[31]

The highest occupied Kohn-Sham state of ${Te_{Cd}}^0$ (depicted in Fig. 2) is antibonding with respect to the axial Te_{Cd}-Te_1 bond. Thus Te_{Cd} is 1.01 Å displaced from the high-symmetry substitutional site and the resulting Te_{Cd}-Te_1 bond is elongated by about 20%.

In the positive charge state, the antibonding ${a_1}^c$ state, with single occupancy, is still in the band gap. However, the distortion is smaller than in the neutral charge state and Te antisite is only 0.61 Å away from the substitutional site. In the double positive charge state, the ${t_2}^c$ defect level is empty and, as expected, there is no Jahn-Teller distortion. Table III gives the details of the geometry of the defect in the three charge states, showing that it is already converged even in the smaller supercells of 64 atoms and splitting the ${t_2}^c$ level into a filled ${a_1}^c$ and an empty e^c state. The ${a_1}^c$ level is antibonding with respect to one of the Te-Te bonds (Fig. 2), which becomes much longer than the other three. In the positive charge state, the ${a_1}^c$ state is only half filled and consequently a smaller distortion is expected. If the defect is double-positively charged, there is no symmetry breaking since the ${t_2}^c$ level is unoccupied and there is no electronic degeneracy.

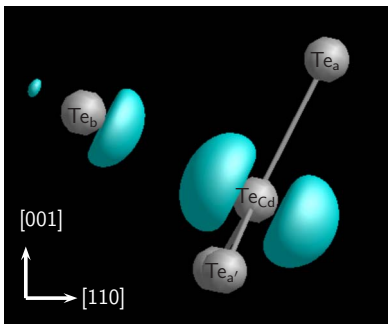

FIG. 2. (Color online) Isosurface of the charge density associated with the ${a_1}^c$ state of ${Te_{Cd}}^0$.

Reorientation

So far, we have considered the static limit valid if the characteristic time of the experiment is much shorter than the reorientation time. The activation energy for defect reorientation can be used to know how the transition rate compares to the characteristic measurement rate.

We analyze the potential-energy surface for the Te antisite determined from first principles. In each cation vacancy cage there are four minima. These are the vertices of a tetrahedron, each one pointing to the center of one of the faces of the larger tetrahedron defined by the original positions of the four Te neighbors. In the adiabatic approximation, the tran-

TABLE III. Equilibrium geometry of the relaxed structure of the Te antisite in different charge states and respective Jahn-Teller energies.

Supercell size		64	216
${Te_{Cd}}^0$	$d(Te_{Cd}\text{-}Te_a)$	3.59	3.63
(C_{3v})	$d(Te_{Cd}\text{-}Te_b)$	2.93	2.94
	ΔE_{JT}	1.04	1.16
${Te_{Cd}}^+$	$d(Te_{Cd}\text{-}Te_a)$	3.32	3.35
(C_{3v})	$d(Te_{Cd}\text{-}Te_b)$	2.93	2.94
	ΔE_{JT}	0.38	0.41
${Te_{Cd}}^{++}$	$d(Te_{Cd}\text{-}Te_a)$	2.96	2.97
(T_d)	ΔE_{JT}	0.00	0.00

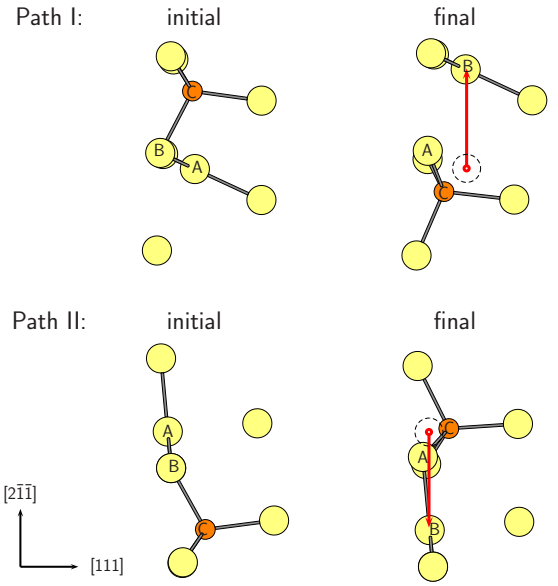

FIG. 3. (Color online) Migration mechanisms investigated for Te_{Cd}. Initial and final states (respectively, before and after a single migration step) are depicted for migration paths I and II. Te and Cd atoms are represented by large and small spheres, respectively. In the representations of the final state, the previous position of the antisite defect and its displacement direction are marked by a dashed circle and an arrow.

sition between two configurations follows the minimum-energy path connecting the two minima and its saddle point occurs when the Te antisite atom is at the mirror plane which transforms the initial into the final configuration. The respective reorientation barriers are 0.13 and 0.42 eV in the single positive and neutral charge states, respectively. These energies are lower than the energy associated with the Jahn-Teller distortion (Fig. 3) because the minimum-energy reorientation path avoids passing through the high-symmetry substitutional site.

C. Formation energies

Both the cadmium vacancy and the tellurium antisite have low formation energies in CdTe. This can be related to the high ionicity and weak bonding comparing to other compound semiconductors.[55] Cadmium vacancy formation energies range from 2.31 eV in Cd-rich material to 1.70 eV in Te-rich material, whereas for the antisite they are limited between 2.74 and 1.54 eV. Since CdTe is usually closer to the Te-rich limit, the concentrations of the two defects will tend to similar equilibrium values. Even if defects are introduced in nonequilibrium conditions, for example, during growth, having such a low formation energy gives an indication that these defects are very likely to form.

Although the convergence of formation energies and transition levels with the supercell size is slower than the convergence of structural parameters, in the 64 atom supercells the formation energies are already converged within 0.1 eV (Tables IV and V). Convergence issues are analyzed in more detail in the Appendix.

TABLE IV. Ionization levels of the tellurium antisite (eV), referenced to the valence-band top. E^{NC} refers to the values obtained without including the Makov-Payne correction. $[E(q/q+1)=E^{NC}(q/q+1)+\Delta\phi_{MP}(q)-\Delta\phi_{MP}(q+1)]$. Experimental values can be found in Table I.

Supercell	64	216
$E^{NC}(0/+)$	0.33	0.30
$E^{NC}(+/++)$	0.37	0.25
$E(0/+)$	0.17	0.19
$E(+/++)$	Below E_v	Below E_v
$\Delta\phi_{MP}(1)$	0.158	0.106
$\Delta\phi_{MP}(2)$	0.632	0.424

D. Ionization levels

The Cd vacancy has two acceptor levels in the gap. Their positions, obtained from Eq. (4), are listed in Table VI. The $E(-/0)$ level is rather shallow, about 0.1 eV above the valence-band top. This transition energy is already converged for the 64 atom supercell. The $E(=/-)$ level is deeper, at about $E_v+0.4$ eV. However, the position of this level converges slower due to the q^2 dependence of the contribution of the spurious electrostatic interaction between the charged defects and the neutralizing background (see Appendix). It is possible that the Makov-Payne correction overestimates the image-charge effects for the doubly charged defect[56] in which case the first and second ionization levels are actually closer.

Another point to give consideration is the band-gap underestimation associated with the local-density approximation (LDA) approximation and the consequent impact on the calculated defect levels. There is not a universal rule for the shift experienced by the levels that lie inside the band gap and different first-principles and semiempirical extrapolation schemes often lead to conflicting results.[57–59] However, it is generally accepted that $E(q/q+1)-E_v$ will be less affected by the band-gap error for defect states with greater valence-band character than for very localized defect states with greater conduction-band character. As the acceptor states of V_{Cd} clearly fall on the former case, we expect that their position relative to the valence-band states where they originate from are little affected by the band-gap error.

We now turn to the Te antisite. This defect is a donor with at least two charge states (neutral and single positive). The

TABLE V. Formation energies of the neutral V_{Cd} (Te-rich material), calculated with different supercell sizes and number of BZ sampling points. The results shown were obtained with a set of *dddd* basis functions for Cd. All values are given in electron volt.

Cell size	BZ sampling	$E_f(V_{Cd}^0)$	$E_f(Te_{Cd}^0)$
64	2^3	1.77	1.56
216	2^3	1.75	1.54
216	Γ	1.64	1.46
512	Γ	1.70	1.51

TABLE VI. Ionization levels of the cadmium vacancy (eV), referenced to the valence-band top. E^{NC} refers to the values obtained without including the Makov-Payne correction. $[E(q/q+1)=E^{NC}(q/q+1)+\Delta\phi_{MP}]$. Experimental values can be found in Table I.

	Calc.	
Supercell size	64	216
$E^{NC}(=/-)$	0.00	0.04
$E^{NC}(-/0)$	−0.04	−0.01
$\Delta\phi_{MP}(q=1)$	0.158	0.106
$E(=/-)$	0.47	0.36
$E(-/0)$	0.12	0.10

thermodynamic (0/+) level is found to be at $E_v+0.2$ eV. The large structural relaxation of the neutral charge state lowers the position of the level by about 0.66 eV comparing to the level obtained for the system restricted to T_d symmetry. The (+/++) level is found to lie just a few millielectron volts below E_v and therefore, taking into account the uncertainty of the calculations, we cannot rule out the existence of a ++ charge state in high-conductivity *p*-type material.

The donor state of Te_{Cd} originates from conduction-band states. Nevertheless, it is very localized (Fig. 2). Thus, an upper bound for $E(0/+)$ can be obtained by applying a rigid shift with the conduction-band states. Following this reasoning, the (0/+) level should not lie higher than $E_c-0.41$ eV. It is not then a shallow donor but a deep center.

E. Migration and defect annealing

Most defect reactions are diffusion limited. If the temperature is enough low, the defects may be preserved by potential-energy barriers which limit the mobility. To predict the stability of intrinsic defects in a nonequilibrium system governed by kinetic processes, it is useful to analyze the defect migration paths.

We determined the minimum-energy paths and the respective saddle points using the climbing nudged elastic band (NEB) method.[60] The migration path is described by a discrete set of intermediate structures $\mathbf{Q}_i$ with $i=1,\ldots,N-1$, named images. We have used five images ($N=4$) in the calculations. As a starting point, we set up the initial and final structures ($\mathbf{Q}_0$ and $\mathbf{Q}_N$, respectively) and obtain the a chain of intermediate images by linear interpolation of $\mathbf{Q}_0$ and $\mathbf{Q}_N$. The minimum-energy path is found iteratively. Each pair of successive images is coupled by a virtual elastic band and the atoms of each image are moved until the forces vanish. After three iterations of the regular NEB method, the highest energy image was allowed to move along the direction of the band (climb) to make sure that the saddle point was found.

1. Cadmium vacancy

The diffusion of the vacancy proceeds by a series of jumps between cation sites. In the most stable charge state in intrinsic and *n*-type material ($V_{Cd}^{=}$), a direct jump to the nearest site of the cation sublattice (the second-nearest-neighbor atom) has an activation energy of 1.19 eV. A migration step along a ⟨100⟩ direction to one of the second-nearest sites of the cation sublattice requires an activation energy of 2.22 eV. An alternative mechanism for migration to the nearest cation site involving a concerted movement of the chain of nearest atoms, intermediated by the formation of a Te_{Cd}-Cd_{Te} pair was also investigated but can be ruled out due to its high activation energy (3.69 eV).

2. Tellurium antisite

The loss of Te_{Cd} is likely to occur by migration followed by trapping at other defects or impurities rather than by dissociation ($Te_{Cd}\rightarrow Te_i^{++}+V_{Cd}^{=}$) since the dissociation reaction is energetically unfavorable with an energy balance of 1.58 eV.

We found two possible migration paths for Te_{Cd}, labeled path I and path II. Each migration step, either along path I or path II, leaves the defect in a different Cd cage but in the same orientation as in the initial configuration. However, the relative orientation of the planes defined by the three nearest neighbors of the Te antisite in the initial and final positions are different in the two cases. The two possibilities considered here are depicted in Fig. 3. Path I leaves the defect in a final position where the plane of its three nearest neighbors is parallel to, but not coincident with, the plane defined by the three nearest neighbors of the defect in its initial position. This migration step involves the passage of a Cd atom through the interstices while the atom originally at the antisite moves to the second-nearest anion site. In contrast, a migration step following path II, starting with the defect at an initial position where its three nearest neighbors are in a (111) plane, leads to a final state with the defect in an equivalent position where its three nearest neighbors are in the same (111) plane (apart from the local relaxation of the Te atoms in the plane). When performing a migration step along path II, the Te atom originally at a Cd site kicks out one of its neighbors which in turn moves to the Cd site.

Both mechanisms involve overcoming a single energy barrier. In the neutral charge state, there is a clear preference for path I with an activation energy of 1.16 eV in detriment of path II with an activation energy of 1.63 eV. In the singly positive charge state, the activation energies are very similar (1.95 and 1.87 eV for path I and path II, respectively). The double positive charge state is the most stable against diffusion, having a migration energy of 2.51 eV. Paths I and II become in this case equivalent.

IV. INTERACTION WITH Zn IN Zn-DOPED CdTe

We start by examining the changes induced by the presence of Zn atoms at the local neighborhood of the defect in the dilute alloy limit ($x\rightarrow 0$). First, the energy associated to the binding between Zn and V_{Cd} or Te_{Cd} is evaluated. Subsequently, we will investigate the repercussion on the defect dynamics.

A. Defect-Zn binding energies

Although isovalent with cadmium, zinc has different ionic size and electronegativity. Hence, its presence changes the

energy necessary to form intrinsic defects in the neighborhood. In the $x \to 0$ limit, the length of the bonds between Zn and its nearest-neighbor Te atoms is 2.640 Å, 12% longer than its ideal, strain-free value in ZnTe. The local tensile strain field close to the Zn substitution plays against the formation of tensile defects while favoring the formation of compressive defects.

In bulk CdTe, the removal of a Cd atom, leaving a cation vacancy, leads to an inward relaxation of the nearest Te atoms and also of the next Cd shell. The distortion increases with the number of electrons at the defect. In $V_{Cd}^{=}$, the Cd-Te bonds in the nearest shell are shortened by 1.6%, whereas in the next shell the remaining bonds are 1.1% than in bulk. Thus, the vacancy also induces a tensile stress field (starting at the next cation shell). Accordingly, the formation of $V_{Cd}^{=}$-Zn_{Cd} pairs is energetically unfavorable. The closest pair formed by placing $V_{Cd}^{=}$ and Zn_{Cd} at the nearest cation sites is 160 meV higher in energy than the infinitely separated pair.

The strain field induced by the Te antisite is more complex. The Te-Te bonds are longer than equilibrium Cd-Te bonds. The Te_a atoms and their neighbors move outward from the center while the Te_b atoms move inwards. On the Te_a side, the defect exerts compressive stress on the surrounding lattice. However, in the neutral charge state, the energy gain achieved by bringing a Zn_{Cd} atom to a position close to Te_a (with Zn and Te_{Cd} in the same mirror plane) is very small: only ~50 meV, close to the accuracy limit of our calculations.

The Zn atoms induce further symmetry lowering at local level. For simplicity, we consider only one Zn atom in the nearest-neighbor cation shell. In the perturbed tetrahedral cage, the four orientations of Te_{Cd} become inequivalent. However, the shape of the potential-energy surface for the Te antisite remains almost unaltered by the Cd↔Zn substitution. The calculated energy of the three inequivalent orientations was identical within ±0.03 eV. Reorientation barriers will also vary little (0.42–0.51 eV). The highest activation energy in this range (0.51 eV) is obtained when the Zn atom is on the reorientation plane, as in that case the Te_{Cd}-Zn bond length is stretched close to the saddle point for reorientation. These results suggest that there is no marked qualitative difference between the reorientation dynamics in pure CdTe and CdTe doped with Zn.

B. Local alloy environment and migration paths

The migration barriers are also changed by the local Zn distribution. ZnTe is less ionic than CdTe and is characterized by higher cohesive energy. Zn-Te bonds are thus shorter and stronger then Cd-Te bonds. Hence, the defects will avoid migration paths that require breaking Zn-Te bonds. If the cation site $V_{Cd}^{=}$ moves to is replaced by Zn, the migration energy of the vacancy is increased to 1.53 eV.

The effect on the diffusion energy of Te_{Cd} is similar. Replacing Cd_C [Fig. 3(a)] by Zn, the migration energy of the antisite via path I is increased for all charge states (Tables VII and VIII). The activation energy of path II is also increased if the neutral antisite exchanges places with a Zn atom at the E site [Fig. 3(d)].

TABLE VII. Activation energy (eV) for the migration of V_{Cd} in different charge states q. The migration step corresponds to an exchange with one of its second-nearest neighbors (the closest cation). $W_{mig}(V_{Cd\to Zn})$ represents the activation energy for exchange of a cadmium vacancy and a zinc atom occupying the nearest cation site.

q	$W_{mig}(V_{Cd}^{q})$	$W_{mig}(V_{Cd\to Zn}^{q})$
0	1.00	1.37
−1	1.01	1.39
−2	1.19	1.53

In summary, the effect of Zn will be to stiffen the lattice, raising the energy necessary to displace the defects. This indicates that (i) both Te_{Cd} and V_{Cd} will migrate following Cd-rich paths and (ii) both defects will be less mobile as x increases.

V. ALLOYING EFFECTS IN $Cd_{1-x}Zn_xTe$

So far, we have discussed qualitatively the effects of the change in the local defect environment due to the presence of Zn atoms in the direct neighborhood or in remote regions. However, alloying causes deep changes in the properties of the host crystal and these should be taken into account in a more detailed model of the defect.

To model how alloying effects affect the properties of the intrinsic defects, we will perform first-principles calculations on a series of randomly generated 64 atom supercells. We will start by showing that the method used to sample the configuration space provides a good description of the properties of defect-free $Cd_{1-x}Zn_xTe$ alloys. These include the dependence of the bond lengths on the alloy composition and the formation enthalpies of the random and ordered phases, which can be compared with experimental and theoretical studies.

A. Modeling bulk CdZnTe alloys

The model system consists of $Cd_{32-n}Zn_nTe_{32}$ supercells, generated by choosing randomly the distribution of the n zinc atoms and $32-n$ cadmium atoms in the cation sublattice. Since there is a periodic repetition at the supercell scale, we will call this pseudorandom model. For each

TABLE VIII. Activation energy (eV) for the migration of Te_{Cd} in different charge states q, following path I or path II. The migration step corresponds to an exchange with one of its second-nearest neighbors (the closest cation). The energy of the analogous move if the cation site where the Te antisite defect moves to is originally occupied by a substitutional zinc atom (Zn_{Cd}) is given in parallel.

q	$W_{mig}^{I}(Te_{Cd}^{q})$	$W_{mig}^{II}(Te_{Cd}^{q})$	$W_{mig}^{I}(Te_{Cd\to Zn}^{q})$	$W_{mig}^{II}(Te_{Cd\to Zn}^{q})$
0	1.16	1.63	2.15	1.97
+1	1.95	1.87	2.19	2.07
+2	2.51	2.41	3.02	2.46

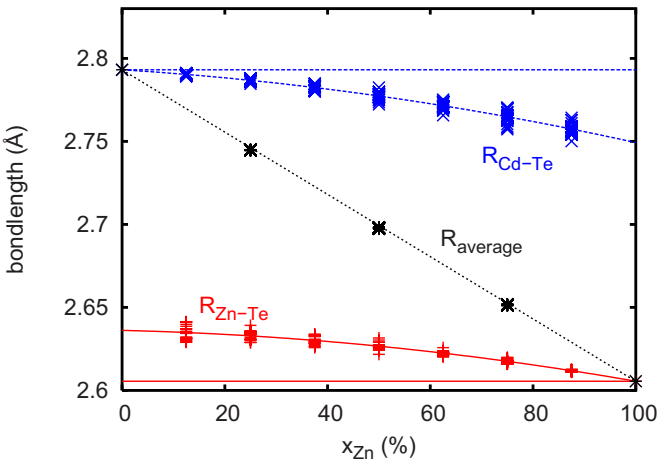

FIG. 4. (Color online) Calculated equilibrium alloy bond lengths $R_{\text{Cd-Te}}$ and $R_{\text{Zn-Te}}$, and average bond length $R_{\text{average}}(x)=\sqrt{a_0(x)}/4$. Each point corresponds to a supercell. Lines are added to aid visualization.

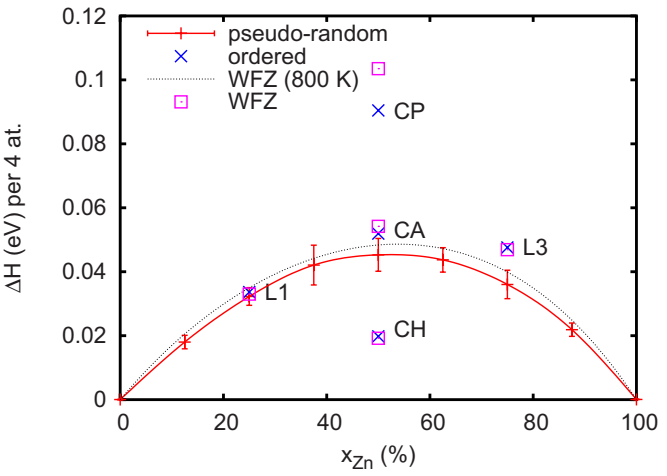

FIG. 5. (Color online) Mixing enthalpy for CdZnTe. Pseudorandom vs ordered structures. The results from the random model and ordered alloy calculations of Wei *et al.* (Ref. 46) are plotted along for comparison.

$n=4,8,12,\ldots,28$, 20 different randomly generated configurations were sampled. Integrations over the BZ were performed using an MP-2^3 scheme. The atomic positions were optimized at constant volume and the equilibrium lattice constant (a_0) was subsequently determined by fitting the Birch-Murnaghan equation of state. The calculated lattice constants are systematically underestimated by about 1%, as typically found by LDA calculations.[38] It is clear that for a given alloy composition, the calculated bond lengths, averaged over the supercell i, vary little with the particular relative positions of the Zn atoms in the supercell (Fig. 4).

The mismatch of the equilibrium Cd-Te and Zn-Te bond lengths ($R_{\text{Cd-Te}}$ and $R_{\text{Zn-Te}}$) leads to a considerable relaxation, in the sense that atomic positions in equilibrium are displaced from the sites of the original zinc-blende lattice. The resulting Cd-Te and Zn-Te bond lengths are closer to the Pauli limit than to Vegard's limit (Fig. 4). The deviation of $R_{\text{Cd-Te}}$ ($R_{\text{Zn-Te}}$) from the CdTe (ZnTe) bond length increases (decreases) nonlinearly with x. The limiting values can be expressed by the relaxation parameters

$$\epsilon_{B\text{-}C}=[R_{BC}(AC{:}B)-{R_{AC}}^0]/({R_{BC}}^0-{R_{AC}}^0), \tag{5}$$

where A and B represent Cd or Zn, and C represents Te, ${R_{AB}}^0$ is the $A-B$ bond length in bulk AB and $R_{BC}(AC{:}B)$ is the $B-C$ bond length around B in the AC host crystal. $\epsilon_{\text{Cd-Te}}$ and $\epsilon_{\text{Zn-Te}}$ are both close to 0.8 (Table II). This is in agreement with experimental evidence and with previous theoretical work.[42,46,61,62]

Despite the rigidity of the bonds, the lattice parameter obeys closely to Vegard's law,[42,46]

$${a_0}^{\text{Vegard}}(x)=x{a_0}^{\text{ZnTe}}+(1-x){a_0}^{\text{CdTe}}, \tag{6}$$

where ${a_0}^{\text{CdTe}}$ and ${a_0}^{\text{ZnTe}}$ are the lattice parameters of CdTe and ZnTe. The deviation from the linear model can be expressed by a parameter γ

$$a_0(x)={a_0}^{\text{Vegard}}(x)+2\gamma x(1-x). \tag{7}$$

A fit of Eq. (7) yields $\gamma\simeq-0.007$ Å, reflecting a very slight downward bending of $a_0(x)$ and resembling the experimental data.[63] As $\gamma\ll a_0$, we will use the lattice parameters obtained from Vegard's law to generate the supercells used for defect models.

We now analyze the preference for ordered alloy structures. Five ordered structures based on the Cd/Zn fcc cation sublattice have been investigated: the Luzonite structures with Zn fractions of 1/4 or 3/4 (labeled L1 or L3, respectively), where the fcc cation sublattice ordering resembles the Cu_3Au structure,[64] the Chalcopyrite (CH) structure, a layered tetragonal (CA) structure, and a layered trigonal (CP) structure, where the fcc sublattice resembles the CuPt structure.[64] These ordering types are described in Ref. 46. The lattice parameters of noncubic CA, CH, and CP structures were optimized using a simplex algorithm.

We compare the energy of the ordered structures with that of the random alloy. The mixing enthalpy for a given concentration can be obtained from comparing the energy of the $Cd_{32-n}Zn_nTe_{32}$ supercell and the energy of supercells of bulk CdTe and ZnTe,

$$\Delta H_{\text{mix}}{}^i(x)=E(Cd_{32-n}Zn_nTe_{32}{}^i)-\frac{32-n}{32}E(Cd_{32}Te_{32})$$
$$-\frac{n}{32}E(Zn_{32}Te_{32}), \tag{8}$$

where i labels a particular alloy configuration (ordered or pseudorandom). For the disordered alloy, it is useful to define an average mixing enthalpy per unit volume which can be compared with the mixing enthalpy per unit cell of ordered configurations. ΔH_{mix} is positive for the CdZnTe ordered and disordered alloys across the whole concentration range. The calculated mixing enthalpies, averaged over the samples, are plotted in Fig. 5 alongside with the results of a previous study using a cluster expansion of the interactions

on the random model.[46] The agreement is excellent, showing that the periodicity arising from the use of a supercell geometry can be disregarded. The formation enthalpy of the ordered alloys was calculated using the same method and is also shown in Fig. 5. The only stable ordered configuration was found to be the chalcopyrite, however the energy difference is so small that it is unlike to drive long-range ordering in the timescale of common preparation procedures. This is in good agreement with the understanding from previous calculations.[46]

Based on the considerations above, we will study the effects of alloying in the intrinsic defects using the pseudorandom-alloy model. This will be presented in Sec. V C.

B. Effect of local strain on the formation of defects

We have shown that one of the effects of alloying is the change in the lattice parameter. This leads to frozen-in stress fields that affect directly the energy necessary to form an intrinsic defect in a particular neighborhood. Aiming at a better understanding of the effect of the local strains induced by the size mismatch on defects outside the range of direct interaction with Zn atoms, we have studied the effect of applying hydrostatic pressure to the embodying CdTe lattice.

The cadmium vacancy keeps its tetrahedral geometry and is rather stiff, presenting less volume deformation than the host matrix. In contrast, the configuration of the Te antisite is sensitive to stress. The relative displacement of the antisite atom along the C_{3v} is increased by the compression of the lattice and the other axial Te atom, labeled Te_b in Fig. 2, is also displaced in the same direction as the stress increases. The reorientation energy is also slightly lowered.

Compressive strain influences the relative concentration of the two defects. The formation of vacancies is favored upon compression but Te_{Cd} becomes progressively less stable. This effect can be quantified by fixing the chemical potential of Te to that of an unstrained precipitate (Te-rich conditions) and obtaining μ_{Cd} from the thermodynamic stability condition for strained CdTe, $\mu_{Cd}+\mu_{Te}=E(CdTe^{\varepsilon})$. The formation energies obtained in these conditions are plotted in Fig. 6. For a compressive strain of $\varepsilon=2\%$, the difference between the formation energies of V_{Cd} and Te_{Cd} increases by about 1 eV.

Pressure has a similar effect in the three charge states of V_{Cd}, having only a minor impact on its energy levels, which remain at a constant distance from the valence-band states where they originate from. The donor level of the Te antisite, however, moves closer to the valence band as the lattice spacing decreases and the Jahn-Teller distortion stabilizes the neutral charge state relative to the positive charge state.

Comparing the results presented in this section with those of Sec. IV A, we find that in dilute $Cd_{1-x}Zn_xTe$ the decrease in the lattice parameter due to the presence of Zn in regions remote to the defect compensates the effect of the presence of Zn in the neighborhood of the defect. As we will show in the next section, the effect of the changes to the average volume dominates in the $x<0.5$ regime.

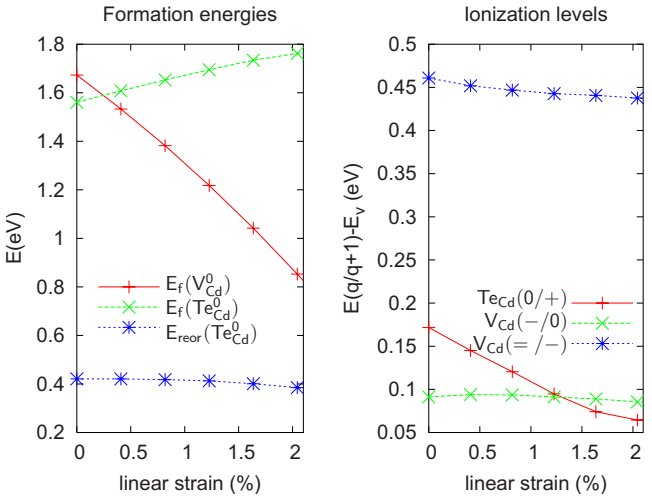

FIG. 6. (Color online) Formation energies (left) and ionization levels (right) of intrinsic defects in strained CdTe, as a function of the linear compressive strain, defined as $\varepsilon=(a_0^{CdTe}-a_0)/a_0^{CdTe}\times 100$. The reorientation energy of the Te antisite is also shown $[E_{reor}(Te_{Cd}^{0})]$.

C. Evolution of the defect properties with the alloy composition

We now consider explicitly the disorder, band-structure changes, and other mixing effects in $Cd_{1-x}Zn_xTe$ by using the pseudorandom-alloy model described in Sec. V A.

1. Defect formation energies

The formation energy of the V_{Cd} and Te_{Cd} defects in $Cd_{1-x}Zn_xTe$ with intermediate compositions ($x=25\%$, 50%, and 70%) was calculated by sampling 15 pseudorandom-alloy configurations, represented by $Cd_{1-n}Zn_nTe$ supercells, where a cation atom was replaced by one of the intrinsic defects. Since this kind of study is very computationally demanding, we used 64 atom supercells, which guarantee a good compromise between accuracy and calculation time. For completeness, we have extended the study up to the ZnTe end point.

The defect formation energies are calculated by computing the difference between the energy of a supercell i with a given distribution of n Zn atoms before and after the replacement of a cation atom by a defect,

$$\Delta E_f^i(x) = E(Cd_{32-n}Zn_nTe_{32}{}^i{:}D) - E(Cd_{32-n}Zn_nTe_{32}{}^i) + \mu_X - \delta\mu_{Te}, \quad (9)$$

where $\delta=1$ for $D=Te_X$, $\delta=0$ for $D=V_X$, and μ_X is the chemical potential of the element replaced. The results show clearly that the total energy depends more on the Zn concentration than on the positions occupied by the Zn atoms in the lattice. Thus, although only a small fraction of all the possible configurations is sampled, we can obtain qualitative results that show the x dependence of the formation energies and defect levels.

The formation energy of the defect depends on the cation species that initially occupied the site. Thus, V_{Cd} and V_{Zn} (and Te_{Cd} and Te_{Zn}) have different formation energies, re-

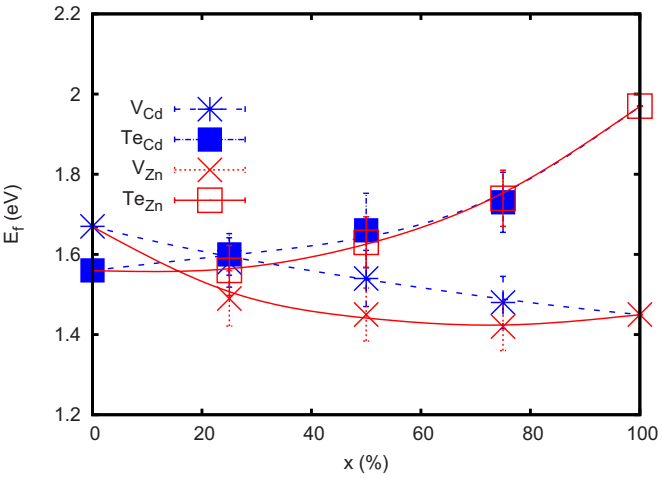

FIG. 7. (Color online) Minimum formation energies of the neutral cation vacancy (V_X) and tellurium antisite (Te_X) defects in $Cd_{1-x}Zn_xTe$ alloys with different Zn concentrations, obtained for Te-rich conditions and for $\mu_X+\mu_{Te}=E(X\text{Te})$. Curves were added to help visualization.

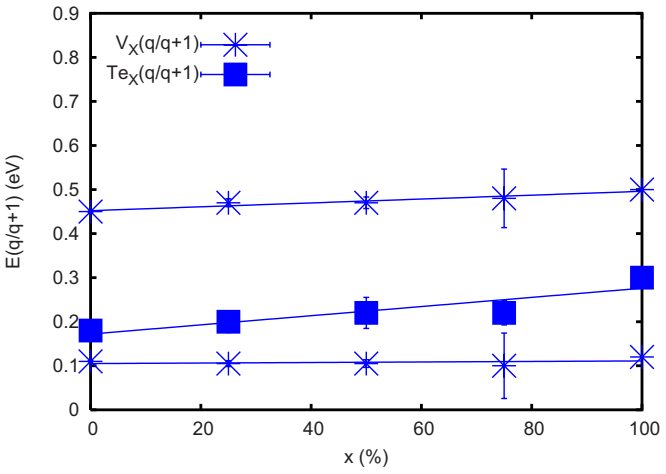

FIG. 8. (Color online) Energy levels of the cation vacancy (V_X) and tellurium antisite (Te_X) defects in $Cd_{1-x}Zn_xTe$ for different Zn concentrations. Lines were added to help visualization.

flecting the availability of the two cation species (translated by the explicit dependence of E_f on μ_X) and the stability of the cation vacancy face to a site exchange involving Cd or Zn. In the three-component alloy a range of values is allowed for the chemical potentials. The conditions $\mu_{Cd}+\mu_{Te}=E(\text{CdTe})$ and $\mu_{Zn}+\mu_{Te}=E(\text{ZnTe})$ establish, respectively, lower bounds for μ_{Cd} and μ_{Zn}. Thus, the minimum V_{Cd} formation energy is obtained for $\mu_{Cd}=E(\text{CdTe})-\mu_{Te}$, whereas the minimum V_{Zn} formation energy is obtained for $\mu_{Zn}=E(\text{CdTe})-\mu_{Te}$. These, along with the minimum Te_{Cd} and Te_{Zn} formation energies, are shown in Fig. 7 for Te-rich conditions.

The formation energy of the neutral V_{Zn} in ZnTe is 0.2 eV lower than the formation energy of V_{Cd} in CdTe, in agreement with previous calculations.[34] In the alloy, there is a smooth variation in the vacancy formation energies between these two end values but with a slight deviation from the linearity. This possibly reflects the behavior of the cohesive energy of the CdZnTe alloy, which is lower than expected from a linear interpolation of the cohesive energy of the two end materials. In contrast, the formation energy of the Te antisites, defects originating an effective outwards expansion of the neighboring atomic shells, has a very different behavior. It is higher in ZnTe than in CdTe, which has a higher lattice constant. Further, comparing the minimum formation energies of V_{Cd} and V_{Zn}, we note that less energy is required to remove the smaller Zn atom than to remove the larger Cd atom in equivalent conditions. Although the difference is within the error bars, it probably results from the size mismatch between Cd and Zn. Theoretically, the formation energy of Te_{Cd} deviates from Te_{Zn} by the same value as for the respective vacancies and the difference between the calculated curves is within the uncertainty range.

2. Transition levels

The ionization levels of the defect do not depend on the species originally occupying the site. In practice, the calculations reveal small differences (of less than 0.06 eV) due to finite supercell size effects, as replacing a Zn atom by a vacancy effectively reduces the Zn concentration by $\Delta x=1/N$, where $N=32$ is the number of available cation sites in the supercell.

Despite the fluctuations, the results show clearly that the electrical activity of V_X remains almost unaltered through the range of compositions studied. Both its $(-/0)$ and $(=/-)$ are anchored to the valence-band top (Fig. 8). The donor level of Te_X moves away from the valence band in an almost linear fashion, with $\frac{d}{dx}E(0/+)=(0.12\pm0.02)$ eV. This is due to its conduction-band character. However, it moves upward at a much lower rate than the calculated conduction-band minima, probably due to the opposed effect of the reduction in the lattice parameter.

We have discussed in Sec. III D the different impact of the band-gap error on the position of the V_{Cd} and Te_{Cd} levels. However, as the magnitude of the band-gap error is similar for CdTe and ZnTe (Table II), it is expected that the calculation of the derivative with respect to x $[dE(q/q+1)/dx]$ benefits from the cancellation of errors, conferring it a higher accuracy than to the $E(q/q+1)$ values themselves.

VI. DISCUSSION

A. Identification of defect signatures

We have shown that the Cd vacancy and the Te antisite have comparable formations energies in Te-rich conditions. A higher concentration of free holes, released by Cd vacancies, favors the formation of Te_{Cd}^{+} while rising the Fermi energy increases the concentration of vacancies. This will result in a balance between the concentrations of the two defects. Furthermore, in intrinsic conditions, the activation energies for migration of the two defects will be both similar and close to $\sim$1.1 eV, drawing a common stability limit for both of them. It is thus not surprising that the identification of their specific signatures has so far been difficult.

Regarding the Cd vacancy, our results confirm the belief that V_{Cd} is one of the major causes of the electrical compen-

sation and carrier trapping observed in CdTe-based detectors. The calculated (=/−) level is close to the thermal ionization energy determined using thermoelectric-effect spectroscopy in CdZnTe with 12% of Zn.[14] It is also consistent with the activation energy of the EPR center observed by Meyer *et al.* (0.47 eV). However, it is difficult to conciliate the structure of this EPR center with the properties of V_{Cd}^{-}.

In fact, we found no measurable Jahn-Teller distortion within the accuracy of our calculations. Thus, even if there is symmetry lowering, the associated energy will be very small, allowing the vacancy to easily recover T_d symmetry by thermal motion at low temperature. This is in agreement with the conclusions of previous first-principles calculations and PAC spectroscopy studies.[25] However, it is in conflict with the assignment of a trigonal EPR center to V_{Cd}^{-}. An alternative explanation could be that this center would be related to the Te antisite or to a divacancy.

Several defect centers observed in Te-rich material have been tentatively assigned to the Te antisite. A study using EPR combined with photoexcitation and modulated-photocurrent spectroscopy has assigned to Te_{Cd}^{+} an isotropic defect, showing superhyperfine interaction with 12 equivalent Cd neighbors and a level at about $E_c-0.2$ eV.[21] This defect has also been assigned to the F center[17] or to an oxygen-containing complex.[22,23] These properties are not inconsistent with those of the Te antisite. The small reorientation energy of the + state (0.13 eV) could explain the isotropy and the creation of the paramagnetic state by 1.4 eV illumination could be explained by an excitation of a donor with a (0/+) level 0.2 eV above the valence band, as suggests the interpretation in Ref. 17. We also point an alternative interpretation by noting a correspondence of its symmetry and the electronic properties to those of V_{Cd}^{-}, which is neutral in intrinsic material and could be activated by light excitation following $V_{Cd}^{=} \rightarrow V_{Cd}^{-}+e^{-}$, corresponding to a $\sim$1.2 eV transition.

Another model based on the interpretation of electrical measurements places the (0/+) and (+/++) levels of Te_{Cd}, respectively, at $E_c-0.01$ and $E_c-0.75$ eV.[13] Although, having into account the band-gap underestimation, we cannot rule out a relation between the $E_c-0.75$ eV level and the (0/+) transition of Te_{Cd}, our calculations suggest that the shallow donor (at $E_c-0.01$ eV) is associated with a different defect, possibly the Cd interstitial.

Additionally, we suggest that the reorientation of Te_{Cd} defects may be in the origin of polarization switching phenomena observed in Zn-doped CdTe materials.[6–9] The stable charge states in CdTe and $Cd_{1-x}Zn_xTe$ are neutral and single positive, and in those states the defect is polar and can be reoriented by the action of an external electric field. Therefore, the off-centrality of Te_{Cd} can serve as a building brick for order-disorder ferroelectricity. However, in this context it is not obvious why the introduction of Zn would lead to the observation of ferroelectricity, unless this is linked to the processing conditions and resulting higher nonstoichiometry of the alloy as compared with CdTe grown by similar techniques.

B. Defect evolution and impact on the conductivity of CdZnTe crystals

Due to their low formation energies, V_{Cd} and Te_{Cd} are the dominant intrinsic defects in CdTe and $Cd_{1-x}Zn_xTe$ grown in Te-rich conditions. V_{Cd} compensates *n*-type dopants, whereas Te_{Cd} compensates *p*-type dopants, limiting the doping efficiency and both may act as recombination centers decreasing the carrier lifetime.

The dependence of the defect formation energies with the Zn content sheds some light on the electrical properties of as-grown dilute $Cd_{1-x}Zn_xTe$ alloys. In CdTe, the formation energy of Te_{Cd} is found to be slightly lower than that of V_{Cd} but a higher Zn/Cd concentration ratio favors the formation of cation vacancies while hindering the formation of tellurium antisites. It has been observed that $Cd_{1-x}Zn_xTe$ with different Zn concentrations display different resistivities and even different conduction type.[13] While as-grown CdTe and very dilute $Cd_{1-x}Zn_xTe$ ($x<0.07$) is *n* type, $Cd_{0.9}Zn_{0.1}Te$ grown under similar conditions is *p* type.[13] This evolution of the conductivity is consistent with the higher concentration of Cd vacancies expected in $Cd_{1-x}Zn_xTe$ with larger x. With low energy for the first ionization, they contribute to the conduction by releasing free holes to the valence band. On the other hand, the compensation by Te_{Cd} donors decreases as their formation energy is higher in the alloy than in the bulk material. The calculated ionization energy of the cation vacancy and its dependence in x is very close to a dominant acceptor level in CdZnTe, measured to vary between 0.12 and 0.13 eV in the CdTe-rich end to 0.15 eV at the ZnTe-rich end[65] and yielding a good agreement with hole mobility data,[66] which possibly corresponds to this defect.

VII. SUMMARY

We have performed a study of the properties of the cadmium vacancy and tellurium antisite in CdTe and CdTe:Zn based on first-principles calculations. Further, our analysis was extended to CdZnTe alloys using a pseudorandom model. In CdTe, V_{Cd} was found to be a double acceptor, with $E(=/-)=E_v+0.36$ eV and $E(-/0)=0.10$ eV. Its first acceptor level is very shallow, with strong valence-band character. No measurable distortion from T_d symmetry was found for the neutral or single positive charge states.

Te_{Cd} exists in the neutral and positive charge states and possibly also in the double positive charge state. The (0/+) level was found to be deep in the band gap and not higher than $E_c-0.4$ eV. An interesting feature of the defect is the spontaneous distortion to C_{3v} symmetry arising from the Jahn-Teller effect. This distortion stabilizes the neutral defect by about 1 eV, driving the donor levels into the lower half of the band gap, not close to the conduction band as has often been assumed. We hope that this information obtained from this study will help to clarify the interpretation of the EPR and PAC spectroscopy data and stimulate further investigation, providing a first step toward the understanding of the more complex scenario in CdZnTe alloys.

With recourse to a study of the defect-Zn interactions in the $x \rightarrow 0$ composition limit and a pseudorandom-alloy model it was possible to establish some general trends. The occu-

pation of the neighboring cation sites with Zn increases the energy necessary to create a cation vacancy. The reduction in the lattice parameter with x has the opposite effect, contributing to the overall decrease in the formation energy of V_{Cd} with increasing Zn content. In contrast, the formation energy of Te_{Cd} increases with Zn content. This is consistent with the higher incorporation of in-grown acceptors in CdTe doped with Zn.[13]

ACKNOWLEDGMENTS

A.C. thanks the University of Exeter for providing computational time. This work was supported by the Swiss National Science Foundation.

APPENDIX: CONVERGENCE CRITERIA

In order to guaranty that the results of the first-principles calculations are independent of the underlying approximations, there are several convergence criteria that must be addressed: these include the cutoff in the Fourier expansion of the charge density, the number of Gaussian basis functions, the mesh of k points used to sample the Brillouin zone, and the size of the supercell.

Starting with the unitary cells of CdTe and ZnTe and a generous **k**-point sampling scheme (MP-8^3), we first evaluate the completeness of the real-space and reciprocal space basis sets. The energy cutoff was set to 112 Ha, and the total energy and lattice parameter change only by 0.006 Å and −0.000027 Ha if this value is increased to 200 Ha.

For the expansion of the Kohn-Sham orbitals we employed an uncontracted basis set consisting of Gaussian functions centered at the atomic sites. The form of the basis functions and the notation used here are defined in Ref. 40. The exponents of the Cd and Te basis functions were optimized for CdTe whilst the exponents of the Zn basis functions were optimized for ZnTe. the exponents of the Zn basis functions were optimized for ZnTe. Since the semicore d states of Cd and Zn are treated explicitly, the inclusion of Gaussian-type orbitals with $l=2$ with several different exponents is required. Thus, while for the Te atoms a *pdppp* basis (including functions with momentum up to d on the second exponent and up to p in the other exponents, corresponding to a total of 26 functions per Te atom) already provided a good expansion, for Cd and Zn we used larger basis sets of *ddddd* and *dddd* type, respectively, which provide a total of 40 and 50 functions per atom. The calculated lattice parameter obtained for CdTe with this choice of basis functions is 6.447 Å deviating only 0.4% from the experimental value at 25 °C.[44]

With the purpose of studying the convergence of the formation energies and energy levels with the supercell size, we also performed calculations with a *dddd* set of basis functions centered on Cd. This allowed an increase in the size of the system up to 512 atoms with a little compromise of the accuracy: with the Cd-*dddd* basis set the calculated lattice parameter of CdTe is 6.427 Å, 0.7% smaller than the experimental value. In the 64 atom supercells, the formation energy of the Cd vacancy is increased by 0.1 eV when replacing the *ddddd* basis set by the *dddd* basis set. This change is comparable to the magnitude of the error arising from finite-size effects.

TABLE IX. Formation energies of the neutral V_{Cd} in Te-rich conditions, calculated with different supercell sizes and number of BZ sampling points, with and without correction for the band-filling error [respectively, noted $E_f(V_{Cd}^0)$ and $E_f^{f-c}(V_{Cd}^0)$]. The results shown were obtained with a set of *dddd* basis functions for Cd. All values are given in electron volt.

Cell size	BZ sampling	$E_f(V_{Cd}^0)$	$E_f^{f-c}(V_{Cd}^0)$
64	2^3	1.77	1.66
216	2^3	1.75	1.72
216	Γ	1.64	1.64
512	Γ	1.70	1.70

Finite size effects

Artificial effects associated with the interaction between defects in neighboring supercells and spurious electrostatic terms figuring in the total energy of charged supercells may converge slowly with the supercell size and it is important to ensure that they do not compromise the accuracy of the calculated defect properties.

For charged systems, there is a spurious effect arising from the electrostatic interaction between the charged defects and the neutralizing jellium background.[67] This spurious electrostatic term scales as q^2 and becomes important for double-charged systems. Several recipes to compute a post-processing correction to the total energy $[\Delta\phi(q)]$ have been proposed and there is no unanimity about which one produces a faster convergence of E_f with increasing system size.[51,56,68–71] In this work, we have adopted the first-order correction proposed by Makov and Payne,[67]

$$\Delta\phi_{MP} = \frac{q^2\alpha_M}{2KL}, \tag{A1}$$

where K and α_M are the dielectric permittivity and Madelung's constant and L is the cubic root of the supercell volume.

The extent to which the calculated properties are affected by spurious defect-defect interaction depends on the extension of the defect wave function. In particular, the fact that the highest unoccupied level of V_{Cd}^0 is very delocalized raises concern about the influence of spurious interactions between defects in different supercells. We addressed this issue by calculating the structure and formation energy of the defect in supercells of different sizes and using different BZ sampling schemes. The results are shown in Table IX. With an identical BZ sampling scheme, the formation energy of the defect varies little when the supercell size is increased. However, there are still differences of about 0.1 eV between the results obtained in the 216 atom supercell using Γ or MP-2^3 sampling.

The use of multiple **k** points for sampling in general compensates the dispersion of the filled Kohn-Sham defect-

localized states and the resulting total energy, averaged over the BZ, converges faster with the supercell size. A denser BZ sampling also provides a better description of the host matrix and consequently of the stress the defect is subjected to. However, in the case of the neutral V_{Cd}, the two holes should be placed in the top of the valence band. If multiple **k** points are used however, the hole is smeared according to the respective weights, increasing the calculated formation energy. These band-filling effects are typical of shallow centers and have been discussed, for example, in Refs. 51 and 56. It has been proposed that the magnitude of the associated error can be estimated by averaging the differences between the energy of the unoccupied Kohn-Sham states and the energy of the bulk valence-band top as suggested in Ref. 56. We compare the convergence of the corrected and uncorrected formation energies with the supercell size and number of points used to sample the BZ in Table IX. Although the correction is slightly overestimated for small supercells, we found that the band-filling correction improves the convergence and therefore it was applied throughout this study. The Te_{Cd} defect has a rather deep band with little dispersion and therefore does not give rise to filling related problems.

[1] F. V. Wald, Rev. Phys. Appl. **12**, 277 (1977).
[2] S. Shwartz, R. Weil, M. Segev, E. Lakin, E. Zolotoyabko, V. M. Menon, S. R. Forrest, and U. EL-Hanany, Opt. Express **14**, 9385 (2006).
[3] T. Aramoto, S. Kumazawa, H. Higuchi, T. Arita, S. Shibutani, T. Nishio, J. Nakajima, M. Tsuji, A. Hanafusa, T. Hibino, K. Omura, H. Ohyama, and M. Murozono, Jpn. J. Appl. Phys., Part 1 **36**, 6304 (1997).
[4] R. W. Birkmire and E. Eser, Annu. Rev. Mater. Sci. **27**, 625 (1997).
[5] P. Fougères, L. Chibani, M. Hageali, J. M. Koebel, G. Hennard, A. Zumbiehl, P. Siffert, and M. Benkaddour, J. Cryst. Growth **197**, 641 (1999).
[6] R. Weil, R. Nkum, E. Muranevich, and L. Benguigui, Phys. Rev. Lett. **62**, 2744 (1989).
[7] L. Benguigui, R. Weil, E. Muranevich, A. Chack, E. Fredj, and A. Zunger, J. Appl. Phys. **74**, 513 (1993).
[8] D. J. Fu, J. C. Lee, S. W. Choi, S. J. Lee, T. W. Kang, M. S. Jang, H. I. Lee, and Y. D. Woo, Appl. Phys. Lett. **81**, 5207 (2002).
[9] I. Stolichnov, E. Colla, N. Setter, T. Wojciechowski, E. Janik, and G. Karczewski, Phys. Rev. Lett. **97**, 247601 (2006).
[10] C. Szeles, S. E. Cameron, S. A. Soldner, J.-O. Ndap, and M. D. Reed, J. Electron. Mater. **33**, 742 (2004).
[11] G. Li, X. Zhang, W. Jie, and C. Hui, J. Cryst. Growth **295**, 31 (2006).
[12] A. Castaldini, A. Cavallini, B. Fraboni, P. Fernandez, and J. Piqueras, Appl. Phys. Lett. **69**, 3510 (1996).
[13] M. Chu, S. Terterian, D. Ting, C. C. Wang, H. K. Gurgenian, and S. Mesropian, Appl. Phys. Lett. **79**, 2728 (2001).
[14] C. Szeles, Y. Y. Shan, K. G. Lynn, A. R. Moodenbaugh, and E. E. Eissler, Phys. Rev. B **55**, 6945 (1997).
[15] C. Szeles, IEEE Trans. Nucl. Sci. **51**, 1242 (2004).
[16] M. A. Berding, Phys. Rev. B **60**, 8943 (1999).
[17] B. K. Meyer, P. Omling, E. Weigel, and G. Müller-Vogt, Phys. Rev. B **46**, 15135 (1992).
[18] B. K. Meyer and D. M. Hofmann, Appl. Phys. A: Mater. Sci. Process. **61**, 213 (1995).
[19] D. M. Hofmann, B. K. Meyer, T. Pawlik, P. Alteheld, and J.-M. Spaeth, Mater. Sci. Forum **143-147**, 417 (1994).
[20] P. Emanuelsson, P. Omling, B. K. Meyer, M. Wienecke, and M. Schenk, Phys. Rev. B **47**, 15578 (1993).
[21] D. Verstraeten, C. Longeaud, A. B. Mahmoud, H. J. von Bardeleben, J. C. Launay, O. Viraphong, and P. C. Lemaire, Semicond. Sci. Technol. **18**, 919 (2003).
[22] P. Fochuk, R. Grill, and O. Panchuk, J. Electron. Mater. **35**, 1354 (2006).
[23] S. A. Awadalla, A. W. Hunt, K. G. Lynn, H. Glass, C. Szeles, and S. H. Wei, Phys. Rev. B **69**, 075210 (2004).
[24] M. Illgner and H. Overhof, Phys. Rev. B **54**, 2505 (1996).
[25] S. Lany, V. Ostheimer, H. Wolf, and Th. Wichert, Physica B **308-310**, 958 (2001).
[26] S. S. Chern, H. R. Vydyanath, and F. A. Krögner, J. Solid State Chem. **14**, 33 (1975).
[27] N. Krsmanovic, K. G. Lynn, M. H. Weber, R. Tjossem, T. Gessmann, C. Szeles, E. E. Eissler, J. P. Flint, and H. L. Glass, Phys. Rev. B **62**, R16279 (2000).
[28] U. Reislöhner, J. Grillenberger, and W. Witthuhn, J. Cryst. Growth **184-185**, 1160 (1998).
[29] A. Castaldini, A. Cavallini, B. Fraboni, P. Fernandez, and J. Piqueras, J. Appl. Phys. **83**, 2121 (1998).
[30] R. Soundararajan, K. G. Lynn, S. Awadallah, C. Szeles, and S.-H. Wei, J. Electron. Mater. **35**, 1333 (2006).
[31] S.-H. Wei and S. B. Zhang, Phys. Rev. B **66**, 155211 (2002).
[32] S. Wei, S. B. Zhang, and A. Zunger, J. Appl. Phys. **87**, 1304 (2000).
[33] Y.-C. Chang, R. B. James, and J.-W. Davenport, Phys. Rev. B **73**, 035211 (2006).
[34] P. Jakubas and P. Boguslawski, Phys. Rev. B **77**, 214104 (2008).
[35] M. Fiederle, C. Eiche, M. Salk, R. Schwarz, K. W. Benz, W. Stadler, D. M. Hofmann, and B. K. Meyer, J. Appl. Phys. **84**, 6689 (1998).
[36] P. R. Briddon and R. Jones, Phys. Status Solidi B **217**, 131 (2000).
[37] M. J. Rayson and P. R. Briddon, Comput. Phys. Commun. **178**, 128 (2008).
[38] J. Heyd, J. E. Peralta, G. E. Scuseria, and R. L. Martin, J. Chem. Phys. **123**, 174101 (2005).
[39] C. Hartwigsen, S. Goedecker, and J. Hutter, Phys. Rev. B **58**, 3641 (1998).
[40] J. P. Goss, M. J. Shaw, and P. R. Briddon, Top. Appl. Phys. **104**, 69 (2007).
[41] J. P. Perdew, K. Burke, and M. Ernzerhof, Phys. Rev. Lett. **77**, 3865 (1996).
[42] M. K. Rabadanov and V. I. Simonov, Crystallogr. Rep. **51**, 778 (2006).
[43] H. Duan, X. Chen, X. Zhou, Y. Huang, L. Sun, and W. Lu, Phys. Rev. B **76**, 035209 (2007).
[44] *II-VI and I-VII Compounds; Semimagnetic Compounds*, Landolt-

Bornstein Group III Condensed Matter, II-VI and I-VII Compounds, Semimagnetic Group, Vol. 41B, edited by U. Rössler (Springer, Berlin, 1999).
[45] *CRC Handbook of Chemistry and Physics*, 75th ed., edited by D. R. Lide (CRC, Boca Raton, 1994).
[46] S.-H. Wei, L. G. Ferreira, and A. Zunger, Phys. Rev. B **41**, 8240 (1990).
[47] M. van Schilfgaarde, T. Kotani, and S. Faleev, Phys. Rev. Lett. **96**, 226402 (2006).
[48] M. van Schilfgaarde, T. Kotani, and S. V. Faleev, Phys. Rev. B **74**, 245125 (2006).
[49] S.-H. Wei and A. Zunger, Appl. Phys. Lett. **72**, 2011 (1998).
[50] J. Coutinho, V. J. B. Torres, R. Jones, and P. R. Briddon, Phys. Rev. B **67**, 035205 (2003).
[51] C. G. Van de Walle and J. Neugebauer, J. Appl. Phys. **95**, 3851 (2004).
[52] S. Lany and A. Zunger, Phys. Rev. B **72**, 035215 (2005).
[53] T. Chanier, I. Opahle, M. Sargolzaei, R. Hayn, and M. Lannoo, Phys. Rev. Lett. **100**, 026405 (2008).
[54] Spin-orbit interaction removes partially the degeneracy of the t_2 state, leaving a fourfold degenerate state in the band gap (Ref. 33). Although the latter is still sensitive to Jahn-Teller effect, no trigonal or tetragonal distortion has been reported in agreement with our results.
[55] N. E. Christensen, S. Satpathy, and Z. Pawlowska, Phys. Rev. B **36**, 1032 (1987).
[56] S. Lany and A. Zunger, Phys. Rev. B **78**, 235104 (2008).
[57] S. Lany and A. Zunger, Phys. Rev. Lett. **98**, 045501 (2007).
[58] A. Janotti and C. G. Van de Walle, Phys. Rev. B **76**, 165202 (2007).
[59] F. Oba, A. Togo, I. Tanaka, J. Paier, and G. Kresse, Phys. Rev. B **77**, 245202 (2008).
[60] G. Henkelman, B. P. Uberuaga, and H. Jónsson, J. Chem. Phys. **113**, 9901 (2000).
[61] V. Koteski, H. Haas, E. Holub-Krappe, N. Ivanovic, and H.-E. Mahnke, J. Alloys Compd. **371**, 138 (2004).
[62] J. L. Martins and A. Zunger, Phys. Rev. B **30**, 6217 (1984).
[63] N. Motta, A. Balzarotti, P. Letardi, A. Kisiel, M. T. Czyzyk, M. Zimnal-Starnawska, and M. Podogorny, J. Cryst. Growth **72**, 205 (1985).
[64] Z. W. Lu, S.-H. Wei, A. Zunger, S. Frota-Pessoa, and L. G. Ferreira, Phys. Rev. B **44**, 512 (1991).
[65] R. Triboulet, G. Neu, and B. Fotouhi, J. Cryst. Growth **65**, 262 (1983).
[66] O. P. Malyk, Physica B **404**, 5022 (2009).
[67] G. Makov and M. C. Payne, Phys. Rev. B **51**, 4014 (1995).
[68] C. W. M. Castleton, A. Höglund, and S. Mirbt, Phys. Rev. B **73**, 035215 (2006).
[69] D. Segev and S.-H. Wei, Phys. Rev. Lett. **91**, 126406 (2003).
[70] T. R. Paudel and W. R. L. Lambrecht, Phys. Rev. B **77**, 205202 (2008).
[71] A. Gali, T. Hornos, N. T. Son, E. Janzen, and W. J. Choyke, Phys. Rev. B **75**, 045211 (2007).